

MATERIALS MICROSTRUCTURE CHARACTERIZATION USING HIGH RESOLUTION TIME-OF-FLIGHT NEUTRON DIFFRACTION

G.D. BOKUCHAVA

Frank Laboratory of Neutron Physics, Joint Institute for Nuclear Research, 141980 Dubna, Russia
E-mail: gizo@nf.jinr.ru

Received September 22, 2015

The neutron diffraction has a great potential for microstructure characterization of various constructional materials due to high penetration power of neutrons and non-destructive character of the method. Using time-of-flight (TOF) technique at pulsed neutron sources allows to record complete diffraction patterns in wide range of interplanar spacing at fixed scattering angles and to analyze polycrystalline materials with complex structures. In current paper a brief overview of some typical examples of materials microstructure investigations by means of TOF neutron diffraction is given. The experiments were performed on the Fourier diffractometers FSD and HRFD at the IBR-2 fast pulsed reactor in FLNP JINR (Dubna, Russia).

Key words: neutron diffraction, peak broadening, microstructure, microstrain, crystallite size.

1. INTRODUCTION

Physical properties of crystalline and, in particular, nanostructured materials are largely dependent on their microstructure, *i.e.* the grain size, the number and type of defects, residual stresses, presence of impurity phases, topology of grain boundaries, the crystallographic texture, etc. Various technological processes used in industry during manufacture and mechanical treatment of materials and products often lead to the formation of complex fields of internal residual stresses, preferred orientation of crystallites (texture), various defects of the crystal lattice, etc. Without detailed information about these phenomena, it is impossible to predict or explain physical, thermal and mechanical properties of materials. Since the reliable methods of predicting microstructural parameters of materials are practically absent, their experimental investigation is of great importance for materials science. In turn, knowledge of the microstructural properties is often used to tailor the required thermal and mechanical properties of modern constructional materials.

Diffraction of thermal neutrons is one of the most informative methods when solving many applied engineering and materials science problems, and it has a number of significant advantages as compared to other techniques. The main advantages of this method are deep scanning of the material under study (up to 2 cm for steel) due to high penetration power of the neutrons, non-destructive character of the method, good spatial resolution (up to 1 mm in any dimension), determination of stress distributions for each component separately of the multiphase material (composites, ceramics, alloys, etc.), possibility to study materials microstructure and defects (microstrain, crystallite size, dislocation density, etc.). In combination with the time-of-flight (TOF) technique at pulsed neutron sources, this method allows to determine lattice strains along different $[hkl]$ directions simultaneously, *i.e.* to investigate mechanical anisotropy of crystalline materials on a microscopic scale.

Internal residual stresses existing in a material cause corresponding lattice strains, which, in turn, result in shifts of Bragg peaks in the diffraction spectrum. This yields direct information on changes in interplanar spacing in a gauge volume, which can be easily transformed into data on residual stresses, using known elastic constants (Young's modulus) of a material [1]. Another important possibility gives an analysis of the shape of a diffraction peak (in the simplest case, its width) which can provide data on crystal lattice distortions (microstrains) inside individual grains and grain sizes. The state-of-the art review of the diffraction analysis of crystallite size and lattice strain can be found, for example, in [2]. A conventional approach developed primarily for X-ray diffraction is the harmonic analysis of several diffraction peaks corresponding to different orders of reflection from the same (hkl) plane [3]. Alternative techniques [4], which make it possible to remove restrictions inherent to classical harmonic analysis, have also been created recently. In addition, the authors of [5] have developed methods for analyzing not only diffraction peak shifts caused by oriented microstresses, but also a decrease in the diffraction peak intensity and an increase in the diffuse background, which arise from statistical lattice distortions produced by atom shifts from ideal positions [6]. Another simple approach is based on the analysis of the integral breadths of individual diffraction peaks using Scherrer equation [7] and the Williamson-Hall plot [8], from which microstructure parameters ("average crystallite size" and a "microstrain") can be directly estimated.

Most of these approaches are routinely employed for the analysis of X-ray data. Some investigations are performed on conventional neutron diffractometers using a monochromatic beam where the resolution function $R(Q)$ is usually parabolic with a rapid rise in the range of small Q . As compared to these instruments neutron TOF diffractometers, operational on pulsed sources, have a great potential for the characterization of the microstructure of modern materials. One of the advantages of TOF diffractometers is simplicity of the functional relationship between the instrument resolution $R(Q)$ and the momentum transfer Q ,

which is almost independent on Q within a fairly wide range. Thus, the TOF-diffractometer makes it possible to register a large number of diffraction peaks with the almost similar contribution of the resolution function to their widths.

2. DIFFRACTION PEAK BROADENING EFFECTS

Neutron diffraction method is quite similar to conventional X-ray scattering. However, unlike characteristic X-rays, thermal neutrons possess a continuous (Maxwellian type) energy spectrum. Since the thermal neutron velocity is rather small, the neutron energy (and wavelength, correspondingly) can be analyzed using the TOF method during the experiment performed on a pulsed neutron source. Depending on the neutron wavelength, the diffraction peak position on the time-of-flight scale is determined from the following condition

$$t = L/v = \lambda mL/h = 2mLd_{hkl}\sin\theta/h, \quad (1)$$

where L is the total flight path between the neutron source and the detector; v , λ , and m are the velocity, wavelength, and mass of neutron, respectively; h is Planck's constant; d_{hkl} is the interplanar spacing; and θ is the Bragg angle.

Therefore, in scale of interplanar spacing d_{hkl} the resolution function of the neutron TOF diffractometer is defined by the expression

$$R = \Delta d/d = [(\Delta t_0/t)^2 + (\Delta\theta/\text{tg}\theta)^2 + (\Delta L/L)^2]^{1/2}, \quad (2)$$

where Δt_0 is the neutron pulse width, $t = 252.778 \cdot L \cdot \lambda$ is the total time of flight (in microseconds), λ is the neutron wavelength (in Å). The first term is the time component of the resolution function, *i.e.*, a TOF uncertainty; the second is the geometric component of the resolution function, which characterizes all geometric uncertainties during scattering at different angles; and the third is a flight path uncertainty.

Thus, the neutron instrument resolution is improved if the neutron pulse width decreases and the flight path or scattering angle increases. For neutron sources with a short neutron pulse ($\sim 20 \mu\text{s}/\text{Å}$), the instrument resolution level of $\sim 10^{-3}$ can be obtained at a substantially increased path length (~ 100 m) with a corresponding loss in intensity. For neutron sources with a long neutron pulse (*e.g.*, IBR-2 fast pulsed reactor), such a method is unacceptable. Hence, on the long pulse neutron sources a special purpose correlation technique is used to achieve high resolution on the TOF-diffractometer. In this case, at a comparatively short path length, a multiple decrease in the effective pulse duration is reached using a fast Fourier chopper, which modulates the primary neutron beam intensity, in combination with the reverse time-of-flight (RTOF) method for data acquisition [9]. Thus, using RTOF-method rather high resolution level $\Delta d/d \approx 2 \cdot 10^{-3}$ (for $d = 2 \text{ Å}$ and $2\theta = 140^\circ$) was achieved for the Fourier stress diffractometer FSD [10,

11] at fairly short the flight distance (~ 6.6 m) between Fourier chopper and neutron detector (Fig. 1a).

As a rule, TOF diffractometers exhibit a rather wide range of interplanar spacing and, consequently, possess a large number of simultaneously observed diffraction peaks. In addition, the functional dependence between the diffraction peak width and the interplanar spacing enables one to estimate microstrain and the size of coherently scattering domains (crystallites) in a rather simple way. From formula (2) it follows that the width of diffraction peak as a function of the interplanar spacing d_{hkl} can be written in the following form

$$\Delta d_R^2 = C_1 + C_2 \cdot d^2, \quad (3)$$

where C_1 and C_2 are some constants related to Δt_0 and $\Delta \theta$, respectively, *i.e.* the time and geometric components of the diffractometer resolution function. A routine method for determining these values is a diffraction experiment with standard sample (*e.g.* polycrystals Si, Al_2O_3 , LaB_6 , etc.), which assumes no microstrain and rather large dimensions of the crystallites.

According to Williamson–Hall analysis for real crystals the diffraction peak broadening effect due to the presence of microstrain ε and finite crystallite size $\langle D \rangle$ is expressed by the formula

$$\beta^2 = (2 \cdot \varepsilon \cdot d)^2 + (k \cdot d^2 / \langle D \rangle)^2, \quad (4)$$

where a Gaussian approximation for distribution functions is assumed, $\varepsilon = \Delta a/a$ is the variance of the unit cell parameter (microstrain), $\langle D \rangle$ is the average size of crystallites, k is a dimensionless coefficient close to unity which takes into account the shape of crystallites. Combining the expressions for Δd_R^2 and β^2 the diffraction peak width at half maxima as a function of interplanar spacing can be obtained as

$$\Delta d^2 = C_1 + C_2 \cdot d^2 + C_3 \cdot d^2 + C_4 \cdot d^4, \quad (5)$$

where $C_3 \approx (2 \cdot \varepsilon)^2$ and $C_4 \approx (k / \langle D \rangle)^2$ are contributions to the diffraction peak broadening due to microstrain and finite crystallite size, correspondingly. The dependences $\Delta d^2(d^2)$ will be linear with higher slope as compared to standard sample if the peak broadening is caused by the presence of microstrain only and finite crystallite size effect is negligible (large crystallites). In case of small crystallites, the peak broadening due to size effect is well pronounced and gives characteristic parabolic dependence (Fig. 1b). Accordingly, plotting these dependences in a sufficiently large range of d_{hkl} , one can easily separate contributions to diffraction peak broadening due to microstrain ε and finite crystallite size $\langle D \rangle$ and determine these microstructural parameters independently.

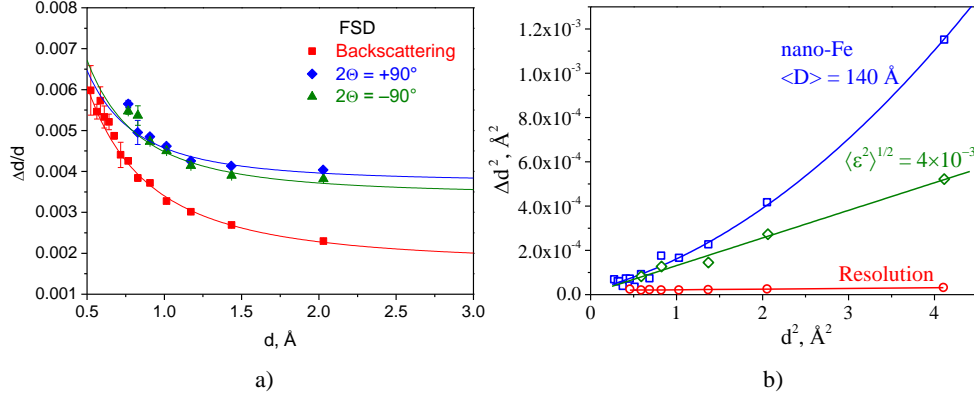


Fig. 1 – a) Resolution function of the FSD diffractometer measured on α -Fe standard powder sample at maximal Fourier chopper speed $V_{\max} = 6000$ rpm. b) Typical dependences of $\Delta d^2(d^2)$ for various materials demonstrating contributions to the diffraction peak broadening due to microstrain ε (straight line) and finite crystallite size $\langle D \rangle$ (parabolic dependence). For comparison, the instrument resolution function is shown.

Microstrain ε and average crystallite size $\langle D \rangle$, which were obtained from analysis of the diffraction peak broadening, can be employed to estimate an important parameter, namely, the dislocation density in the material under investigation. From comparison between the crystal lattice elastic energy per unit volume and the energy of a single dislocation, it was demonstrated [12] that the dislocation density can be estimated as

$$\rho = k \cdot \varepsilon^2 / (F \cdot b^2), \quad (6)$$

where ε is the microstrain, b is the Burgers vector, F is parameter describing the interaction of dislocations (in the simplest case, $F = 1$), and $k = 12 \cdot A$, where $A = 2$ corresponds to the Lorentzian peak shape and $A = \pi/2$, to the Gaussian shape. As a rule, the coefficient k for many materials varies from 2 to 25. With application of the given model, it is assumed that all dislocations contribute to diffraction peak broadening and microstrains are independent of the $[hkl]$ direction in the crystal. In particular, when the Burgers vector of dislocations is oriented along the $[110]$ direction ($F = 1$), it was established that the parameter $k = 16.1$ for the face-centered (FCC) and $k = 14.4$ for body-centered (BCC) cubic lattices.

When the diffraction peak width at half maxima is analyzed with the aim of studying microstrains defined by formula (5), it is convenient to subtract the instrument resolution function and, afterward, examine the diffraction peak broadening β related only to the properties of the material under consideration. Quite often, Williamson–Hall analysis of the interrelation between peak broadening β^2 and d^2 shows that certain $(h00)$ and (hhh) reflections deviate markedly from the linear dependence. Such a deviation is usually associated with

variations in the dislocation contrast factor and has been observed repeatedly during X-ray scattering experiments [13, 14]. The given anisotropic effect can be taken into account using the model suggested by T. Ungár [15] for non-oriented polycrystalline materials with the cubic symmetry. This model combines the modified Williamson-Hall (MWH) and Warren-Averbach (MWA) methods. In this approach the anisotropic diffraction peak broadening depends on the average dislocation contrast factor \bar{C} , which takes into account the orientation and elastic characteristics of dislocations:

$$(\Delta K)^2 = \left(\frac{0.9}{\langle D \rangle} \right)^2 + \frac{\pi M^2 b^2 \rho}{2} K^2 \bar{C} \pm O(K^4 \bar{C}^2), \quad (7)$$

where $K = 2\sin\theta/\lambda = 1/d$ is scattering vector, $\Delta K/K = \Delta d/d$, $\Delta K = (\Delta d/d) \cdot K = \Delta d/d^2$ is the peak width at half maxima, $\langle D \rangle$ is the crystallite size, M is the constant determined by the effective radius of the dislocation cut-off, ρ is the dislocation density, b is the Burgers vector, \bar{C} is the average dislocation contrast factor, and $O(K^4 \bar{C}^2)$ are the higher order residual terms.

In particular, the averaged dislocation contrast factor of a cubic crystal is described by the simple relationship

$$\bar{C} = A - B(h^2 k^2 + h^2 l^2 + k^2 l^2)/(h^2 + k^2 + l^2)^2 = A - BH^2 = \bar{C}_{h00}(1 - qH^2), \quad (8)$$

where h , k , and l are the Miller indices, q is a experimentally determined parameter that depends on the edge or screw character of the dislocations, \bar{C}_{h00} is the average dislocation contrast factor for the $(h00)$ reflection and is determined by the elastic parameters of the material C_{11} , C_{12} and C_{44} [see 15], $H^2 = (h^2 k^2 + h^2 l^2 + k^2 l^2)/(h^2 + k^2 + l^2)^2$ is the orientation factor (anisotropy factor), parameters A and B depend not only on the elastic constants of the material and the effective radius of the dislocation cut-off, but also on whether dislocations are of the edge or screw type. In this case, material microstrains are anisotropic and possess minimum and maximum values at $H^2 = 0$ and 0.33, respectively.

From (7) and (8) equation for diffraction peak broadening can be rewritten as

$$\frac{(\Delta K - \alpha)^2}{K^2} = \delta^2 \bar{C}_{h00}(1 - qH^2), \quad (9)$$

where $\alpha = 0.9/\langle D \rangle$ and $\delta^2 = \pi \rho b^2 M^2/2$.

In addition, from the experimentally determined value of q the ratio between edge or screw dislocations can be found as [16]

$$f_{edge} = \frac{q_{screw} - q}{q_{screw} - q_{edge}} = 1 - f_{screw}, \quad (10)$$

where f_{edge} and f_{screw} are the fractions of edge and screw dislocations, respectively, q_{edge} and q_{screw} are values of q for the pure edge and pure screw dislocations calculated according to [15].

Rather recently alternative WPPM method (Whole Powder Pattern Modelling) was proposed for the retrieval of microstructural information [17, 18]. WPPM method is based on the modelling of the whole diffraction pattern and its distinguishing feature is the generation of the diffraction peak profiles based on physical models of the microstructure and characteristics of the instrument. Within this approach, the microstructure model can involve shape and sizes of the coherently scattering domains, dislocations, stacking and twin faults, etc.

In contrast to previously mentioned methods in WPPM a lognormal distribution of crystallite sizes can be derived from the diffraction data:

$$g(D) = \frac{1}{D\sigma\sqrt{2\pi}} \exp\left[-\frac{1}{2}\left(\frac{\ln D - \mu}{\sigma}\right)^2\right], \quad (11)$$

where μ and σ are adjustable parameters. In this case the volume-weighted average domain size can be calculated from the parameters of the lognormal distribution as [17]: $\langle D \rangle_v = 3/4 \cdot \exp(\mu + 7/2 \cdot \sigma^2)$.

At present, the WPPM method is implemented in the PM2K software package [19], which is mostly used for X-ray data analysis. In the near future, the PM2K software will be updated to allow for a full microstructural analysis from neutron TOF data, giving researchers new additional possibilities.

3. RESULTS AND DISCUSSION

The described above methods are routinely used on Fourier diffractometers for neutron TOF data analysis and to provide important information about materials microstructure. Below some typical examples of microstructure investigations of structural materials by neutron diffraction under various external conditions (uniaxial load, temperature, fatigue cycling, heat treatment, etc.) are given.

3.1. AUSTENITIC STEEL X6CrNiTi1810 UNDER UNIAXIAL LOAD *IN SITU* AND LOW CYCLE FATIGUE PROPERTIES

Austenitic steels enjoy wide commercial application because of their high strength and corrosion resistance. For high-strength material production, of special

interest are such mechanical properties of austenitic steels as creep, formation of new phases, mechanical and thermal fatigue, and peculiarities of fatigue failure under cyclic loads. High-resolution neutron diffraction was used to study the mechanical properties of the X6CrNiTi1810 austenitic steel under uniaxial external load [20] and residual internal stresses due to cyclic fatigue of the material.

The austenitic steel sample was subjected to the external uniaxial load *in situ* in the neutron beam, using stress rig (Fig. 2a). The elastic strain was measured for different crystal planes (hkl) with scattering vector Q direction parallel and perpendicular to the applied load (Fig. 2b). Additionally, the macroscopic sample deformation was determined independently by extensometers from relative changes of sample dimensions. In order to characterize materials anisotropy the lattice strains for all available crystal planes (hkl) were obtained from relative shifts of individual diffraction peaks.

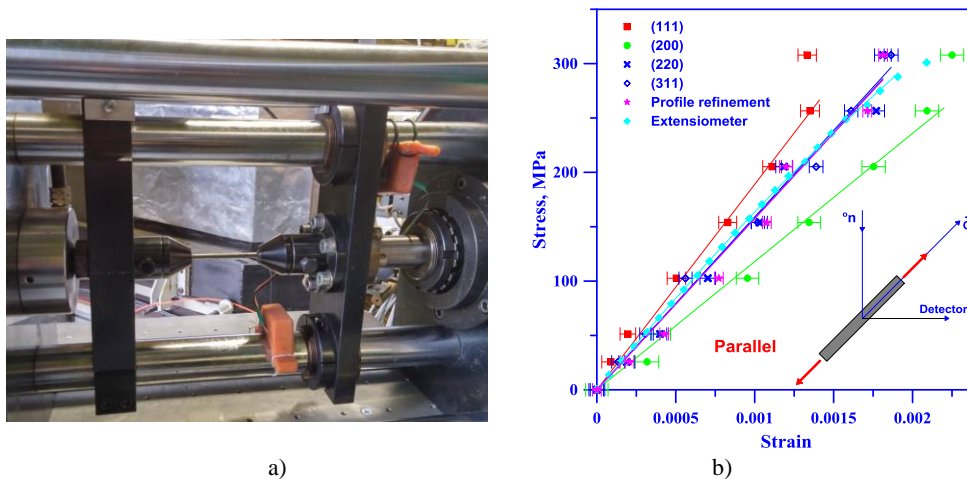


Fig. 2 – a) Uniaxial stress rig (compression/tension) installed on FSD stress diffractometer. b) Crystal lattice strain for different (hkl) reflections measured in direction parallel to applied uniaxial load. Inset shows the scheme of the experiment.

In plastic deformation regime (at the applied stress level $\sigma > 250$ MPa) macroscopic sample deformation registered by extensometers deviates from linear dependence while the lattice strain obtained from neutron diffraction data exhibits more complicated behavior. Thus, tighter lattice planes (hhh) exhibit partial hardening during plastic deformation while compliant planes ($h00$) demonstrate some softening. At the same time, peak broadening behavior during applied load is quite remarkable. The diffraction peak width remains almost constant during elastic load regime ($\sigma < 250$ MPa) while during plastic deformation it increases significantly reflecting the corresponding increase in the microstrain (Fig. 3a). From the slopes of the strain-stress linear dependencies in elastic region the

Young's modulus E_{hkl} and Poisson's ratio ν_{hkl} were obtained for each lattice plane (hkl). Analyzing E_{hkl} and ν_{hkl} as a function of the anisotropy (orientation) factor $\Gamma_{hkl} = (h^2k^2 + h^2l^2 + k^2l^2)/(h^2 + k^2 + l^2)^2$ the elastic stiffness constants C_{11} , C_{12} and C_{44} can be evaluated in the frame of the selected elasticity model (Reuss, Hill, Kröner) (Fig. 3b).

When studying the fatigue properties, a series of cylindrical samples were subject to a various number of tension–compression cycles with a maximum deformation of $\pm 0.6\%$ and a frequency of 0.1 Hz. The experimentally determined number of cycles corresponding to the total material fatigue upon appearance of cracks and initiation of fatigue failure turned out to be equal to $N_{\max} \approx 1020$.

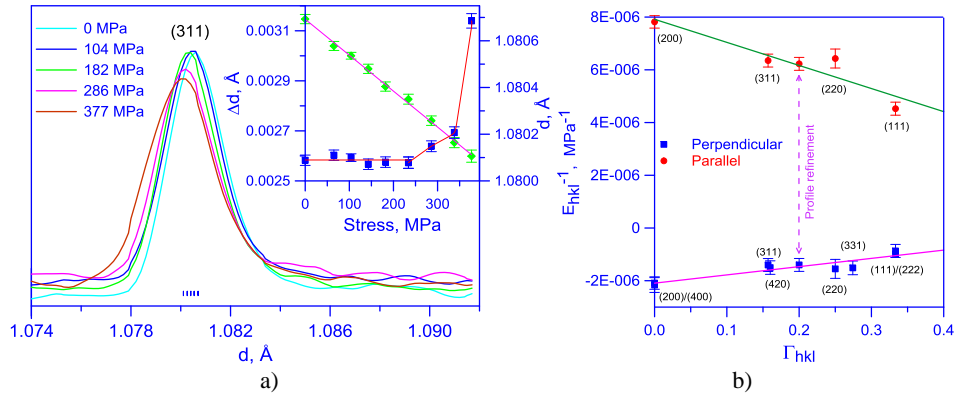


Fig. 3 – a) Diffraction peak (311) shifts and profile changes vs. applied load. Inset shows dependences of diffraction peak (311) position d_{hkl} and width Δd_{hkl} vs. applied load. b) Dependence of the elastic modules E_{hkl}^{\parallel} and E_{hkl}^{\perp} measured in directions parallel and perpendicular to the applied load vs. the anisotropy factor $\Gamma_{hkl} = (h^2k^2 + h^2l^2 + k^2l^2)/(h^2 + k^2 + l^2)^2$.

For samples with different degrees of material fatigue N/N_{\max} , neutron diffraction experiments were conducted in order to determine their phase state and the residual stress level [21]. The diffraction peaks from the initial austenitic phase corresponded to a face-centered cubic (FCC) structure (sp. gr. $Fm\bar{3}m$). With an increasing degree of material fatigue, the appearance of diffraction peaks of a martensitic phase was observed in the neutron diffraction patterns (Fig. 4).

As it is known, austenite undergoes a phase transition to the tetragonal martensitic phase due to thermal treatment or plastic deformation. The tetragonal distortion value for the martensitic structure depends strongly on the carbon content. In our experiment due to low content of carbon (0.04%) in this type of steel tetragonal distortion of the martensite lattice was not observed. Therefore, the observed martensitic phase was considered in the frame of the body-centered cubic (BCC) structure (sp. gr. $Im\bar{3}m$). Usually martensitic phase growth starts at the grain boundaries of the initial austenitic structure. At that, the martensite phase produces

a structure of oriented plates or laths. For this reason martensite texture formation during phase transition can be expected. Indeed, the registered neutron diffraction spectra exhibit weak texture presence and its slight variation with fatigue degree.

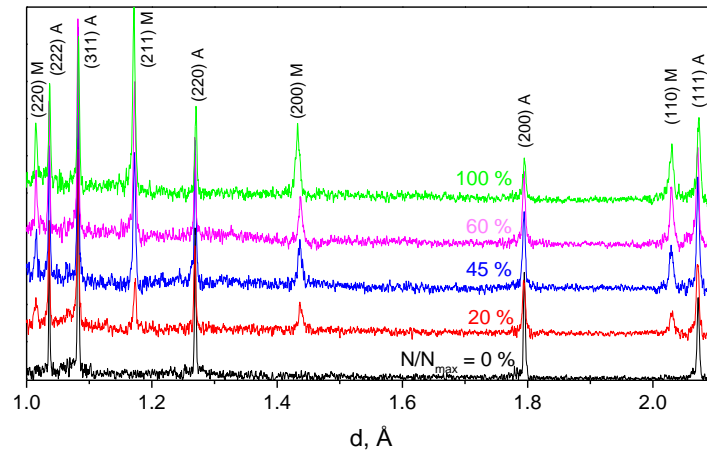


Fig. 4 – Neutron diffraction pattern evolution vs. fatigue degree. Miller indices for austenite (A) and martensite (M) phases are shown.

The residual strain for both phases was measured in the longitudinal and radial directions assuming cylindrical symmetry of the stress field distribution in the sample. For an austenitic matrix, the elastic constants determined from the previous *in situ* experiment with uniaxial load were used and for martensite were taken from the literature [22]. The estimated residual stresses in austenite phase are mainly compressive with maximal amplitude ~ 100 MPa while stresses in the martensite phase are tensile with maximal amplitude ~ 250 MPa (Fig. 5a). Near fatigue failure region ($N/N_{max} = 90\text{--}100\%$) the tendency to redistribution of residual stresses between austenite and martensite phases was observed.

Using simple Williamson-Hall approximation the diffraction peak broadening was analyzed and average microstrain values ε were calculated for both phases. The microstress values were estimated as $\sigma = E \cdot \varepsilon$, where E is Young's modulus for the corresponding phase. The microstress in austenite phase increases at the beginning of the fatigue cycling and then remains almost constant with the increase of number of load cycles. At the same time, for the martensitic phase the microstress behavior depending on the fatigue degree indicates its partial relaxation with increasing number of load cycles. Most likely, this phenomenon is connected with the growth of microcracks in the more brittle martensite structure.

Additionally, the whole profile refinement of the diffraction pattern according to the Rietveld method [23] allowed a quantitative estimate of the volume content for each phase, depending on fatigue degree N/N_{max} (Fig. 5b). Before the fatigue failure, the volume fractions of the austenitic and martensitic

phases become equal, which is responsible for the occurrence of cracks due to strong stress at the phase boundaries.

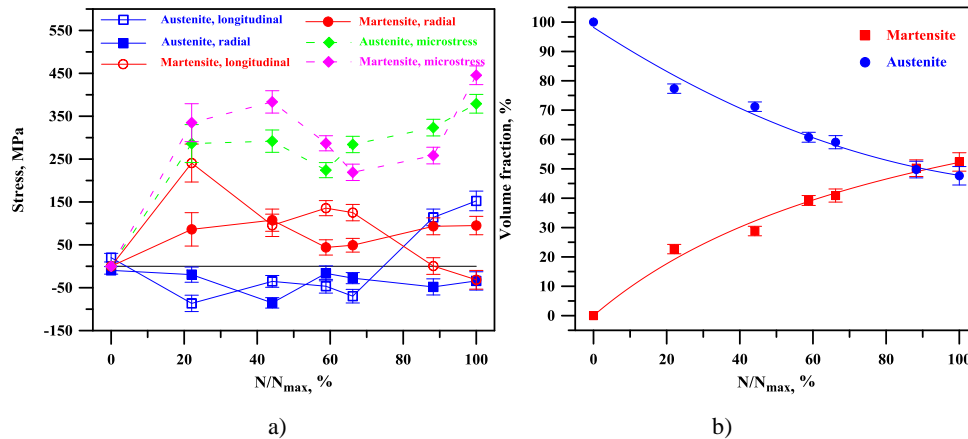


Fig. 5 – a) Residual stresses and microstresses for austenite and martensite phases vs. fatigue degree. b) Austenite and martensite volume fractions derived from Rietveld refinement vs. fatigue degree.

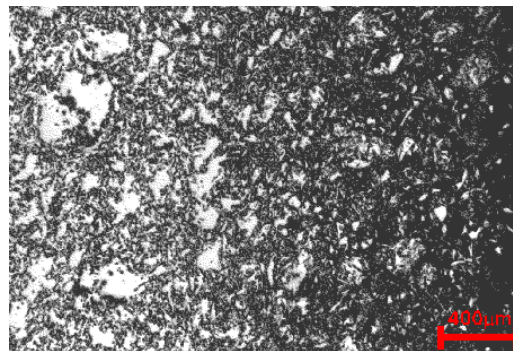
3.2. CERAMIC MATRIX COMPOSITES Al₂O₃/Al

The development of technology for modern materials has led to a new method of producing composite materials in which a metal is infiltrated into a porous ceramic matrix under gas pressure. Brittle ceramic materials are reinforced by the inclusion of an elastic phase, usually by a metal, which enables one to improve the mechanical characteristics of such composites. In this case, the metal is infiltrated into a matrix usually at temperatures slightly higher than the metal melting point. The most typical materials of this kind are composites Al₂O₃/Al, combining materials with very different elastic and thermal properties, in which metal Al phase is infiltrated into a porous ceramic α -Al₂O₃ matrix (Fig. 6a). For example, one can compare the Young's moduli and coefficients of thermal linear expansion of these two materials: $E = 400$ GPa and $\alpha = 8.4 \cdot 10^{-6} \text{ K}^{-1}$ for Al₂O₃, $E = 70$ GPa and $\alpha = 23.1 \cdot 10^{-6} \text{ K}^{-1}$ for Al. Therefore, due to the significant difference in the coefficients of thermal expansion, the metal phase, when cooled, experiences greater compression than the ceramic phase does. For this reason, tensile residual stresses are expected in metal phase, while in ceramics there will be compressive ones.

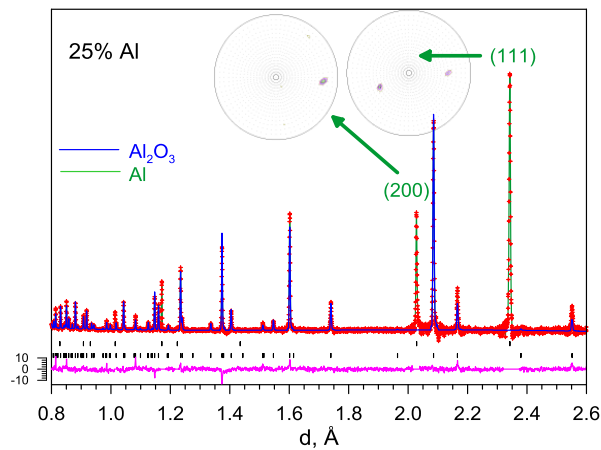
Two series of Al₂O₃/Al composites with an average size of metallic inclusions of 0.1 and 1 μm were investigated by neutron diffraction method [24]. In each of these series, the matrix porosity and, accordingly, the volume fraction of Al phase were 15%, 25%, and 35%. The diffraction patterns of all the samples contained well-resolved peaks of both phases (Fig. 6b). Changes in the lattice

parameters in relation to the content and average size of metal inclusions, as well as corresponding residual strains averaged over all observed reflexes (hkl), were determined by the Rietveld method for the matrix of Al_2O_3 .

In the Al_2O_3 phase, no preferred orientation of crystallites was found, whereas in the Al metal phase there was a strong texture, and therefore the strains were calculated based on the results of processing of individual diffraction peaks. In the composites being studied, the Al_2O_3 phase turns out to be under the action of compressive stress, while the metal phase is under tensile stress (Fig. 7a). The stress in the Al phase decreases with increasing volume fraction and average size of the metal inclusions. The behavior of stress in the matrix is more complicated and strongly dependent on the microstructure of the composite.



a)



b)

Fig. 6 – a) Microstructure of $\text{Al}_2\text{O}_3/\text{Al}$ composite: dark area – Al_2O_3 , light area – Al. b) A part of the neutron diffraction pattern of the composite with 25% of Al (vol. fr.) and average size of metallic inclusions $\sim 1 \mu\text{m}$. Pole figures (111) and (200) for Al phase are shown.

The high resolution of the diffractometer also allowed estimating the microstress level in the material based on a precise analysis of diffraction peak broadening within simple Williamson-Hall approximation. As expected, the residual microstress ($\sigma = E \cdot \varepsilon$) level in both phases of the composite increases almost linearly with increasing content of the Al metal phase (Fig. 7b). The residual microstress level in both phases for a fine-grained structure (0.1 μm) is on average higher than for a coarse-grained one (1 μm).

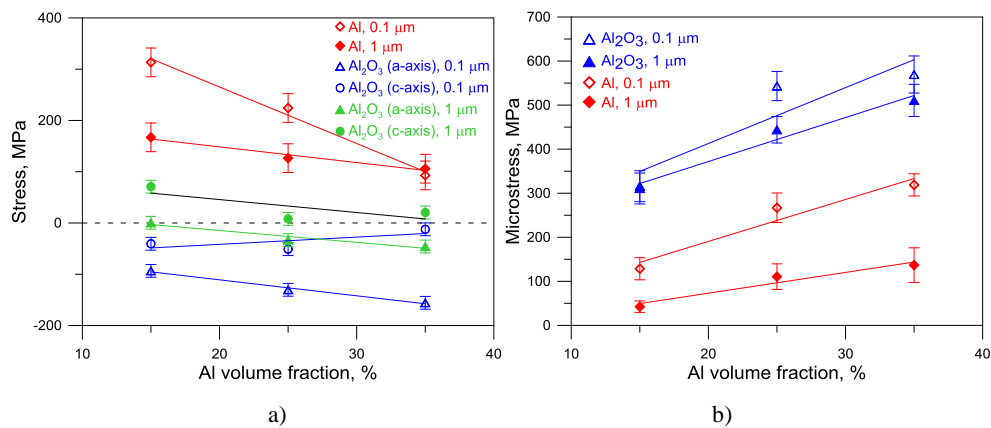


Fig. 7 – Residual stress (a) and microstress (b) in the Al₂O₃/Al composite with fine- and coarse-grained microstructure vs. Al volume fraction.

3.3. PLASTICALLY DEFORMED AUSTENITIC STEEL 16Cr–15Ni–3Mo–1Ti

Modern nuclear industry requires the creation of new radiation-resistant materials (steels and structured alloys) which can operate at high radiation doses and retain their mechanical properties. Mechanical characteristics of materials can be optimized by their chemical composition and microstructure. Fairly often, the manufacturing process causes appearance of residual microstresses and branched dislocation structure due to plastic deformation that significantly affects the properties of material. In turn, irradiation with fast neutrons introduces significant changes in steel microstructure, causing the formation of various types of defects. Therefore, to predict the service life of the nuclear reactor components it is vital to control materials microstructure, which affects strongly its mechanical properties.

Neutron diffraction experiments on the investigation of intermetallic and carbide ageing of the austenitic 26Ni–5Cr–3Ti and 0.40C–4Cr–18Mn–2V steels were performed in [25, 26]. The results of these studies demonstrated that intermetallic or carbide nanosystems formed due to the artificial ageing of steels exert a significant influence on their behavior under irradiation. However, as was

established by studying neutron irradiation effects in pure nickel [27], the development of radiation damages in FCC metals can also depend on the dislocation system formed by mechanical deformation. In current study, the 16Cr–15Ni–3Mo–1Ti austenitic steel was selected for experiments as a best candidate material for the production of fuel-element cladding for fast-neutron reactors. During the first stage of the research, the unirradiated samples of this steel were studied to estimate the neutron diffraction applicability to solving this problem and acquire initial data for the analysis of radiation-induced defects. In further neutron diffraction investigations of the irradiated samples, these data can serve as reference information.

Thus, to investigate how the intrinsic mechanical treatment of austenitic steels affects the irradiation-initiated behavior, 16Cr–15Ni–3Mo–1Ti steel with a low titanium content was chosen and used to prepare samples whose degrees of cold deformation were 10, 20, 30, and 40% [28]. The initial steel was maintained at 1100 °C within 2 hours with subsequent cooling in water in order to obtain a single-phase austenite with a FCC crystal lattice and to relieve residual stresses in the material. Then, the samples were subjected to cold plastic deformation by rolling to a reduction of 10%, 20%, 30%, and 40%. For neutron diffraction experiments the samples were manufactured as cylinders 55 mm long and 6.45 mm in diameter. All main diffraction peaks of the spectra were indicated in the frame of the FCC structure with the space group $Fm\bar{3}m$ and the lattice constant $a_0 \approx 3.6 \text{ \AA}$. The main structural parameters were obtained using profile analysis of the measured diffraction spectra according to the Rietveld method (Fig. 8a). In addition, individual diffraction peaks were processed with the help of the least-squares (LS) method to analyze the dependence between the peak width and the interplanar spacing and to determine how crystal lattice microstrain and the average size of crystallites contribute to the peak width.

The crystal lattice constant depends weakly on the degree of sample deformation, and its absolute value is in good agreement with our previous results obtained in studying the different heat treatment modes of the same steel grade [29, 30]. At the same time, with increasing degree of sample deformation significant broadening of the individual diffraction peaks in the spectra was observed (Fig. 8b), confirming that material microstrain grows within very wide limits.

As is evident from Fig. 9a, where the instrument resolution functions $\Delta d/d$ measured with the help of the standard sample and the studied austenitic steel samples are compared, existing broadening effects can be reliably measured on the FSD diffractometer. The analysis of the peak broadening $\Delta d^2(d^2)$ revealed characteristic deviations from the linear dependence. The effect is more pronounced for certain reflections, namely $(h00)$ and (hhh) . Such a deviation is usually associated with anisotropic microstrain, which is caused by elastic stress

fields near the dislocations in the material. In this case, the anisotropic peak broadening effect is defined by variations in the dislocation contrast factor.

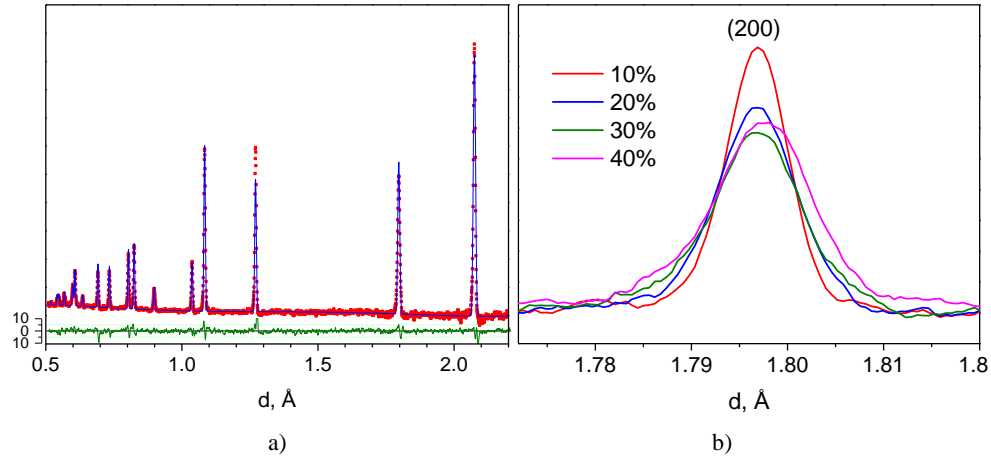


Fig. 8 – a) Neutron diffraction pattern from the sample deformed by 20%. Data were processed by the Rietveld method. Experimental points, calculated profile and difference curve are shown. b) Diffraction peak (200) shape changes vs. plastic deformation degree.

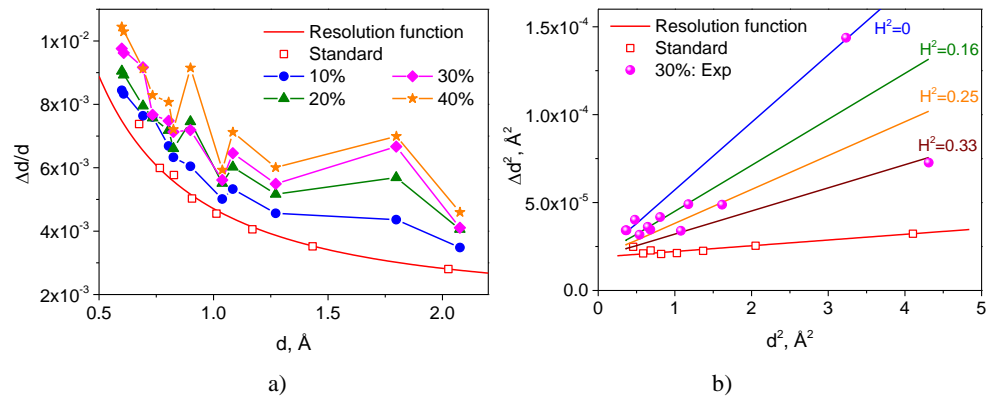


Fig. 9 – a) Resolution function $\Delta d/d$ for all studied samples. For comparison, the instrument resolution function measured with the help of the standard sample is shown. b) The dependence Δd^2 vs. d^2 for the sample with 30% of deformation. The continuous lines were plotted using the LS fitting results and correspond to microstrain with different values of anisotropy factor H^2 .

The study of diffraction peak broadening demonstrated that crystallite sizes contribute negligibly to the peak width. On the contrary, microstrains make the main contribution to the above phenomenon. Using T. Ungár's model [15] the diffraction peak broadening was analyzed and average microstrain values were calculated. The given model based on LS fitting provides a satisfactory description

of the anisotropic diffraction peak broadening. It should be emphasized that the parameters fitted *via* the LS method enabled to construct model curves corresponding to different values of the orientation factor H^2 (Fig. 9b). In this case, the experimental values of the peak broadening β^2 agree very well with the corresponding model curves (Fig. 10a). The dependence of microstrain ε , which is averaged over all orientations and corresponds to $H^2 = 0.2$, is shown in Fig. 10b. Its value increases if the degree of plastic deformation of the material increases. Accordingly, the estimated dislocation density also increases from $1.7 \cdot 10^{14}$ to $6.9 \cdot 10^{14} \text{ m}^{-2}$ (Fig. 11a).

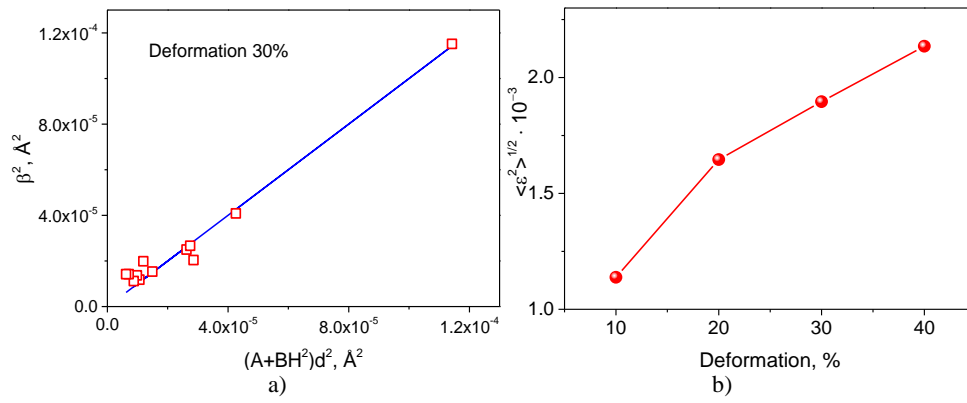


Fig. 10 – a) Squared peak broadening β^2 vs. $(A+B \cdot H^2) \cdot d^2$ at 30% deformation of the sample. Squares designate experimental values, and the continuous line corresponds to the LS fitting. b) Averaged lattice microstrain vs. the plastic deformation degree.

In addition, the aforementioned model can be used to estimate the ratio between edge and screw dislocations in the studied material. For this purpose, the experimentally determined dislocation contrast factor \overline{C}_{h00} should be compared with theoretical values of $\overline{C}_{h00}^{edge}$ and $\overline{C}_{h00}^{screw}$, *i.e.* with the contrast factors of pure edge and pure screw dislocations calculated separately. For the studied 16Cr–15Ni–3Mo–1Ti steel, the results are presented in Fig. 11b. It was found that the fraction of edge dislocations in the material decreases from 75 to 4% with increasing degree of plastic deformation. Accordingly, the fraction of screw dislocations increases under the same conditions. Afterward, the fraction of edge dislocations increases and reaches 28% at the maximum degree of plastic deformation of 40%.

Transmission electron microscopy (TEM) was also used to study the dislocation structure of austenitic 16Cr–15Ni–3Mo–1Ti steel samples *versus* the degree of plastic deformation. For TEM studies the specially prepared foils of $\sim 100 \mu\text{m}$ thickness were used. The bright-field images of the structure, microdiffraction

patterns, and the dark-field images of different reflections were obtained to identify phases. The dislocation densities were determined by means of the secant method.

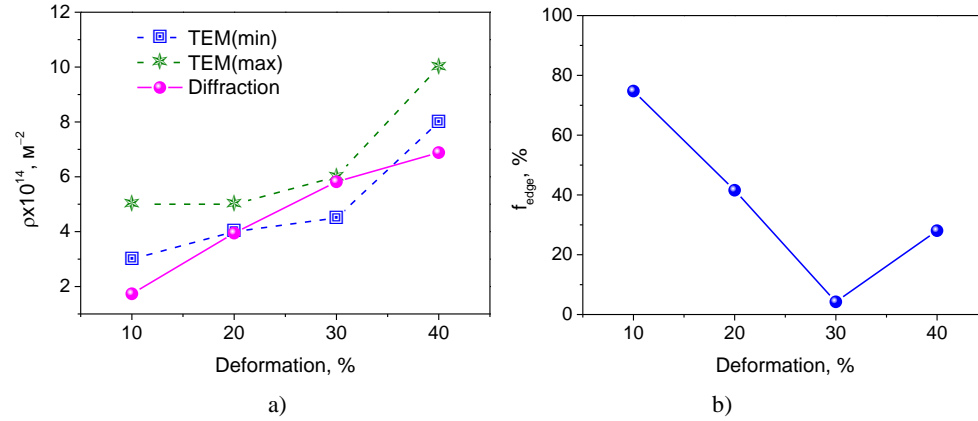


Fig. 11 – a) Dislocation density from neutron diffraction data and TEM.
b) Fraction of edge dislocations in the material.

From the analysis of TEM images it was concluded that the structure of the examined steel samples deformed by 10 and 20% involves only single twins (Fig. 12a). When the degrees of deformation of the material are 30 and 40%, the density of twins grows appreciably (Fig. 12b). It turned out that the dislocation density varies over the grain volume. There are regions with low and high dislocation densities. Most likely, this can be explained by the fact that TEM is a local method employed to investigate separate regions of a thin foil, in which the dislocation density can vary substantially. As opposed to TEM, neutron diffraction data are averaged over the entire volume of the sample under study and provide an integral estimate of the dislocation densities. Moreover, TEM results can be affected by dislocations that are formed on sample surfaces during thin foil preparation. Hence, the dislocation density in foils is smaller as compared to the initial material. However, comparison between the results of both methods indicates that, in our case, the dislocation density estimates determined from the neutron diffraction data coincide closely with the TEM results (Fig. 11a).

Recently [31] the microstructure of plastically deformed steel 16Cr–15Ni–3Mo–1Ti was examined by neutron diffraction and electron microscopy before and after fast-neutron irradiation ($E > 0.1$ MeV) with a fluence of $5 \cdot 10^{19}$ n/cm². The data obtained in this research work confirmed our results for unirradiated samples. It was found that with increasing the degree of cold deformation, the dislocation density grows almost linearly. In cold deformed steel samples after fast neutron irradiation the dislocation density decreases due to the radiation-stimulated diffusion of point radiation defects. This effect occurred more intensively in the samples with higher initial degree of deformation.

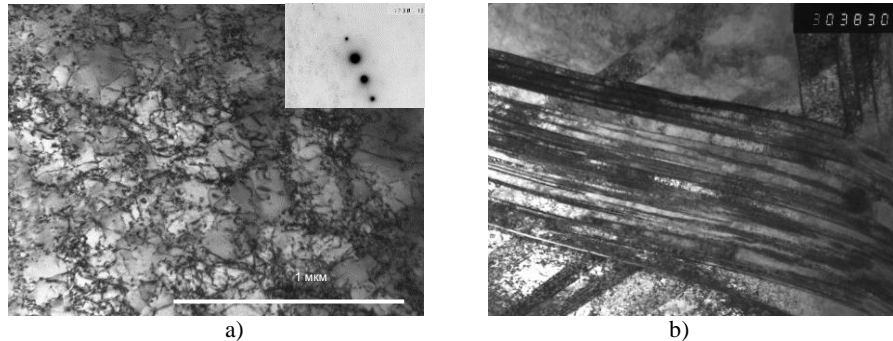


Fig. 12 – TEM images of 16Cr-15Ni-3Mo-1Ti austenitic steel deformed by 10% (a) and 40% (b).

3.4. HEAT TREATMENT OF DISPERSION-HARDENED FERRITE-MARTENSITE STEEL

Heat-resistant pipeline components (elements of steam superheaters, turbine blades, etc.) of thermal power plants operating in the creep conditions at temperatures up to 650 °C are often made from modern tempered ferrite-martensite steels of the P91/P92/P911 grades with approx. 9–10 %wt of chromium content. Therefore, it is important to improve thermal efficiency and mechanical properties of such materials. The heat treatment of tempered ferrite-martensite steel usually consists of two stages: austenization and tempering. It is well known that chromium in steels delays the formation of carbides, and that martensite phase forms in such steels after slow air-cooling. Ferrite-martensite steels have a complex microstructure, which consists of fine micro-grains separated by different kinds of interfaces (grain boundaries, block boundaries and twin boundaries) and precipitate particles of carbonitrides and carbides near these boundaries. Long-term use of such steels at temperatures over 600 °C become possible due to the formation of stable dislocation structure of martensite, which is formed as result of air hardening (normalization) after medium-temperature tempering. The stability of the dislocation structure both during tempering and during creep is ensured by the formation of nano-dispersed particles of Me(C,N) carbonitrides and $Me_{23}C_6$ carbides.

Additionally, these steels exhibit a very high dislocation density after heat treatment. Dislocations are produced in the parent phase during the martensitic transformation due to the associated martensite shear. As it well known from previous research works the dislocation density strongly drops in the early stages of tempering and then gradually decreases with further aging. Ferrite-martensite steels with high dislocation densities exhibit specific mechanical properties. Thus, they show cyclic softening when exposed to strain controlled fatigue testing and a strong decrease of creep rate during primary creep. The decrease of the high dislocation density in such material during tempering and creep accounts for the

formation of subgrain boundaries that represent a dominant feature of ferrite-martensite steel microstructures.

TOF neutron diffraction is a powerful tool for *in situ* investigation of important parameters of materials microstructure such as lattice strain, microstrain and size of crystallites. At the same time, microstrain and crystallite size are closely related to the dislocation structure inside the grain of polycrystalline material, which defines mechanical properties of the steels. Using the modern methods of diffraction peak broadening analysis it is possible to estimate these parameters in real material and study their changes with temperature and external load. The obtained microstructural information is of great importance for better understanding of the heat-resistant properties of investigated steels, as well as high embrittlement at low and high temperatures. This approach gives a possibility to optimize thermomechanical treatment of the steels to improve their properties.

In current study the microstrain and crystal structure of Fe–9%Cr type ferrite-martensite steel in wide range of tempering temperatures was investigated on FSD diffractometer at the IBR-2 pulsed reactor [32]. This steel revealed good results in the long-term heat resistance, which is by about 10% higher as compared with the previously developed steels of this type. This gives hope for its use in thermal power units at supercritical conditions ($P = 30$ MPa and $T = 620$ °C). Initially the samples were normalized at 1050 °C and tempered for 3 hours at temperature of 750 °C. Tempered samples were investigated in two stages: 1) the neutron diffraction spectra were measured in the temperature range from 20 to 600 °C *in situ* from initially quenched samples placed directly into the mirror furnace in the neutron beam (Fig. 13a); 2) the neutron diffraction spectra were measured at room temperature from series of samples after tempering in furnace at temperatures of 500 to 820 °C with subsequent cooling on air.

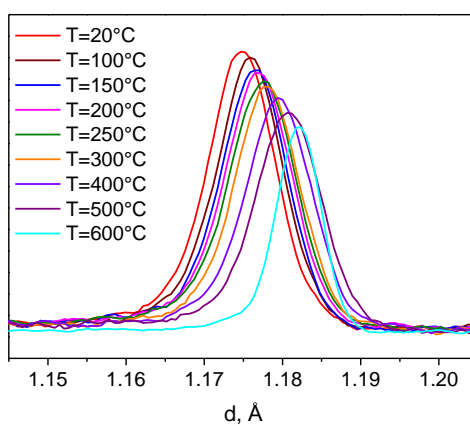
After quenching from normalization temperature, the studied steel exhibits single phase 100% martensite with cubic structure. All main diffraction peaks of the spectra were indicated in the frame of the BCC structure with the space group $Im\bar{3}m$ and the lattice constant $a_0 \approx 2.873$ Å. Traces of residual austenite or δ -ferrite in the neutron diffraction pattern were not found. Despite the high-resolution diffractometer, splitting the individual reflections of the BCC lattice was not observed due to low carbon content. The main structural parameters were obtained using profile analysis of the measured diffraction spectra according to the Rietveld method. In addition, individual diffraction peaks were fitted by least-squares method to analyze peak broadening effects.

The part of neutron diffraction pattern demonstrating (211) reflection shifts and profile changes with temperature is presented in Fig. 13b. It turned out that the

diffraction patterns exhibit very broad reflections up to temperatures of $\sim 500\text{ }^{\circ}\text{C}$ with corresponding sharp decrease in the peak widths at higher temperatures. The lattice parameter dependence *vs.* temperature (Fig. 14a) allowed estimating the linear expansion coefficient of the material, which has a value typical for this class of steels: $\alpha = 11.2 \pm 0.5\text{ }^{\circ}\text{C}$.



a)



b)

Fig. 13 – a) Studied sample in the mirror furnace (1 kW, $T_{\text{max}} = 1000^{\circ}\text{C}$) on FSD diffractometer.
b) Diffraction peak (211) position and shape *vs.* temperature.

The measured diffraction patterns have shown significant diffraction peak broadening in tempered samples as compared with reference material (Fig. 14b). The anisotropic peak broadening effect observed on FSD is expressed quite strongly and can be readily registered due to quite good instrument resolution. Detailed analysis of peak widths revealed anisotropic character of peak broadening

at which some reflection deviate from linearity. For correct microstrain evaluation such peak width anisotropy was considered in the frame of the modified Williamson-Hall model [15] (Fig. 15a).

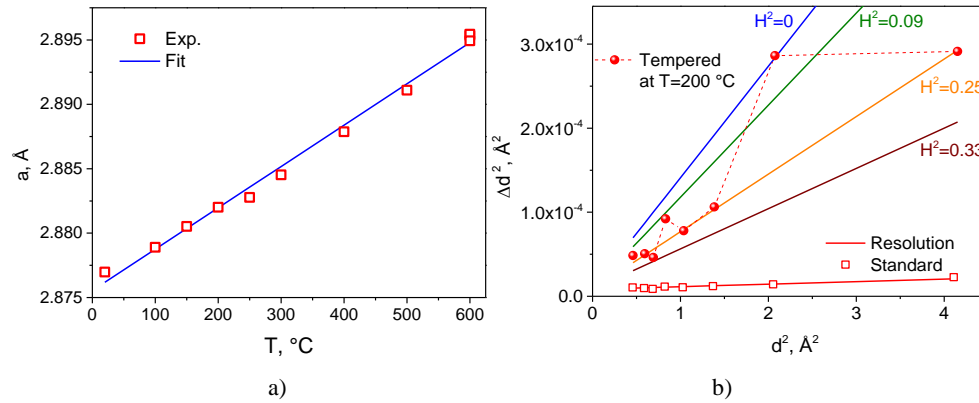


Fig. 14 – a) Lattice parameter vs. temperature. b) Δd^2 vs. d^2 for the ferrite-martensite steel sample tempered at T = 200°C.

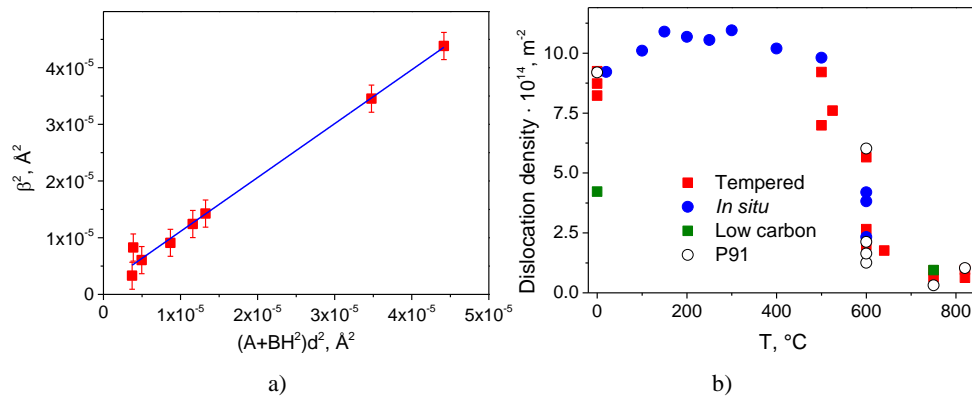


Fig. 15 – a) Fit result of Δd^2 vs. $(A+B \cdot H^2) \cdot d^2$ for the ferrite-martensite steel sample tempered at T = 200°C. b) Dislocation density in ferrite-martensite steel vs. tempering temperature.

The dislocation density was estimated within the above-mentioned model for both sample series: measured *in situ* and tempered. For comparison, the additional experiments were performed with P91 steel and experimental grade of low-carbon ferritic steel which dislocation density data were included in analysis too. Thus, the dislocation density exhibits quite high values and varies slightly in the range $8 \cdot 10^{14} \div 1.1 \cdot 10^{15} \text{ m}^{-2}$ for temperatures from 20 °C up to 500 °C. At temperatures above 500 °C it decreases sharply down to $6.2 \cdot 10^{13} \text{ m}^{-2}$ (Fig. 15b). The similar behavior is observed for P91 and low-carbon steels. The observed sharp decrease in microstrain and dislocation density for temperatures above 500 °C clearly

indicates intensive precipitation of carbonitrides and carbides in the martensite structure that can affect significantly the mechanical properties of the studied steel.

4. CONCLUSIONS

The performed experiments demonstrated that TOF neutron diffraction possesses many advantages and, therefore, can be considered as a suitable tool for the precise characterization of the microstructure of modern constructional materials. The achieved resolution level allows investigating important parameters of materials microstructure such as lattice strain, microstrain and size of crystallites. Available auxiliary equipment (stress rigs, furnaces, etc.) provides wide variability of experimental conditions on the studied sample.

In combination with Fourier correlation technique at long-pulsed neutron source the potentiality of the TOF diffractometry is very high allowing to achieve an extremely high resolution level at relatively short flight path. This contributes to the increase of the neutron flux on a sample and to the reduction of the facility costs. Thus, an optimal balance between intensity and instrument resolution can be reached. Accumulated work experience and developed methods for materials microstructure investigations on such neutron instruments can be successfully used at next-generation high-flux neutron sources with long neutron pulse.

Acknowledgements. This work was supported by Russian Foundation for Basic Research and the Moscow Region Government (project No. 14-42-03585_r_center_a).

REFERENCES

1. A.J. Allen, M.T. Hutchings, C.G. Windsor, *Adv. in Physics*, **34**(4), 445-473 (1985).
2. E.J. Mittemeijer, U. Welzel, *Z. Kristallogr.*, **223**, 552-560 (2008).
3. B.E. Warren, B.L. Averbach, *J. Appl. Phys.*, **2**, 595-599 (1950).
4. J.G.M. van Berkum, *Strain fields in crystalline materials: Methods of analysis based on x-ray diffraction-line broadening: Ph.D. Thesis*, Delft University of Technology, The Netherlands, 1994.
5. M.A. Krivoglaz, *Theory of X-ray and Thermal Neutron Scattering by Real Crystals*, Plenum Press, New York, 1969.
6. M.A. Krivoglaz, *Diffuse Scattering of X-Rays and Neutrons by Fluctuations*, Springer-Verlag: New York, 1996.
7. P. Scherrer, *Nachr. Ges. Wiss. Goettingen, Math.-Phys. Kl.* **1918**, 98-100 (1918).
8. G.K. Williamson, W.H. Hall, *Acta Metall.*, **1**, 22-31 (1953).
9. P. Hiismaki, H. Poyry, A. Tiiitta, *J. Appl. Cryst.*, **21**, 349-354 (1988).
10. G.D. Bokuchava, V.L. Aksenov, A.M. Balagurov, V.V. Zhuravlev, E.S. Kuzmin, A.P. Bulkin, V.A. Kudryashev, V.A. Trounov, *Appl. Phys. A: Mater. Sci. & Process.*, **74** [Suppl1], s86-s88 (2002).
11. [1] G.D. Bokuchava, A.M. Balagurov, V.V. Sumin, I.V. Papushkin, *J. Surf. Invest.: X-ray, Synchrotron Neutron Tech.*, **4**(6), 879-890 (2010).
12. G.K. Williamson, R.E. Smallman, *Phil. Mag.*, **1:1**, 34-46 (1956).

13. T. Ungár, G. Tichy, *phys. stat. sol. (a)*, **171**, 425-434 (1999).
14. J. Pešička, R. Kužel, A. Dronhofer, G. Eggeler, *Acta Mat.*, **51**, 4847-4862 (2003).
15. T. Ungár, I. Dragomir, Á. Révész and A. Borbély, *J. Appl. Cryst.*, **32**, 992-1002 (1999).
16. F. Hajy Akbary, J. Sietsma, A.J. Böttger, M.J. Santofimia, *Mat. Sci. & Eng. A*, **639**, 208-218 (2015).
17. P. Scardi, M. Leoni, *Acta Cryst. A*, **57**, 604-613(2001).
18. P. Scardi, M. Leoni, *Acta Cryst. A*, **58**, 190-200 (2002).
19. M. Leoni, T. Confente, P. Scardi, *Z. Kristallogr.*, **23**(Suppl.), 249-254 (2006).
20. A.M. Balagurov, G.D. Bokuchava, J. Schreiber, Yu.V. Taran, *Phys. B: Cond. Mat.*, **234-236**, 967-968 (1997).
21. G.D. Bokuchava, V.V. Luzin, J. Schreiber and Yu.V. Taran, *Textures and Microstructures*, **33**, 279-289 (1999).
22. F. Bollenrath, V.Hauk and E.H. Miiller, *Z. Metallkunde.*, **58**, 76-82 (1967).
23. H.M. Rietveld, *J. Appl. Cryst.*, **2**, 65-71 (1969).
24. A.M. Balagurov, I.A. Bobrikov, G.D. Bokuchava, V.V. Zhuravlev, V.G. Simkin, *Phys. of Partic. and Nucl.*, **46**(3), 249-276 (2015).
25. V.V. Sagaradze, V.I. Voronin, I.F. Berger, E.G. Volkova, B.N. Goshchitskii, *Phys. Met. Metallogr.*, **112**(5), 517-525 (2012).
26. V.V. Sagaradze, B.N. Goshchitskii, E.G. Volkova, V.I. Voronin, I.F. Berger, A.I. Uvarov, *Phys. Met. Metallogr.*, **111**(1), 80-90 (2012).
27. A.P. Druzhkov, D.A. Perminov and V.L. Arbuzov, *J. Nucl. Mater.*, **430**, 279-284 (2012).
28. G.D. Bokuchava, I.V. Papushkin, V.I. Bobrovskii, N.V. Kataeva, *J. Surf. Invest.: X-ray, Synchrotron Neutron Tech.*, **9**(1), 44-52 (2015).
29. G.D. Bokuchava, I.V. Papushkin, V.V. Sumin, A.M. Balagurov, D.V. Sheptyakov, *Phys. of the Solid State*, **56**(1), 165-169 (2014).
30. G.D. Bokuchava, I.V. Papushkin, V.V. Sumin, D. Aznabayev, B. Mukhametuly, A.M. Balagurov, D.V. Sheptyakov, *Phys. of Partic. and Nucl. Let.*, **10**(2), 157-161 (2013).
31. V.I. Voronin, E.Z. Valiev, I.F. Berger, B.N. Goschitskii, N.V. Proskurnina, V.V. Sagaradze, N.F. Kataeva, *J. Nucl. Mater.*, **459**, 97-102 (2015).
32. G.D. Bokuchava, V.V. Sumin, I.V. Papushkin, Annual Report 2012. Frank Laboratory of Neutron Physics. Joint Institute for Nuclear Research, (2012).